Hybrid MDSOGI–ROGI Control Strategy for Mitigating Harmonics and Unbalance in SEIG Based Standalone Systems

Jotirmoy Samanta, *Associate Member, IEEE,* Ralli Sangno, Rajen Pudur, *Senior Member, IEEE*, Yatindra Gopal, and Julio C. Rosas-Caro, *Senior Member, IEEE*

***Abstract*—The self-excited induction generator (SEIG) is a promising machine for standalone, off-grid systems. However, this machine experiences multiple power quality issues (PQIs) when subjected to varying loads, particularly degradation in terminal voltage and frequency as the load increases. This paper presents a PQI mitigation technique using a shunt active power filter (SAPF) to regulate the terminal voltage of the SEIG and reduce the total harmonic distortion (THD) of the system, while maintaining power factor (PF) close to unity. A modified dual second-order generalized integrator (MDSOGI) is combined with a reduced-order generalized integrator (ROGI) to generate the reference current for controlling the SAPF. The terminal voltage of SEIG is regulated under dynamic load changes. Total harmonics distortion (THD) is reduced below 5% according to the IEEE 519-2022 standard. Furthermore, under an unbalanced load condition, the system becomes balanced after compensation with the SAPF. The experiment is conducted on a real-time platform using Opal-RT (OP4510), and the results of dynamic load changes are presented.**

Link to graphical and video abstracts, and to code: https://latamt.ieeer9.org/index.php/transactions/article/view/10152

***Index Terms*—Self excited induction generator, shunt active power filter, power quality, second order generalized integrator**

I. Introduction

THE increasing focus on renewable energy sources and off-grid systems has highlighted various power quality issues (PQIs) in edge-of-grid systems [1]. Due to its advantages over synchronous generators, the Self-Excited Induction Generator (SEIG) has proven effective for emerging renewable energy applications in remote locations [2]. However, maintaining good power quality in a stand-alone SEIG is a significant challenge, as it experiences voltage regulation issues, frequency fluctuations, reduced power factor (PF), and increased total harmonic distortion (THD) under different loading conditions [3]. In [3], it is inferred that under non-linear loaded conditions, the (5^{th}, 7^{th}, 11^{th}, 13^{th}, 17^{th}) order harmonics affect the SEIG-based off-grid system performance. The voltage regulation of SEIG depends primarily on its excitation capacitance, with delta-connected capacitor configurations proving effective [4], [5]. Reliability assessments indicate that the success and failure probabilities of a three-phase SEIG are 0.5490 and 0.4510, respectively [6]. Several SEIGs with varying higher ratings may be integrated into an edge-of-grid system to improve performance as well as to reduce the burden on lower rated SEIG units [7]. To enhance power delivery along with power quality, single-phase SEIGs have also been integrated with photovoltaic (PV) systems [8], [9]. Despite these advancements, voltage and frequency regulation remain a major problem for SEIG based edge-of-grid systems that are not integrated with certain power electronics converters.

The power electronics converters, such as unified power quality conditioners (UPQC) or static synchronous compensators (STATCOM), can be used to reduce the PQIs that emerge in standalone SEIG [10]–[13]. Such converters typically have a voltage source inverter with a filter inductor on the AC side including a DC-link capacitor on the DC side. While STATCOM-based solutions have effectively addressed dynamic PQIs, their reliance on battery storage increases system costs [14], [15]. As an alternative, SAPF offers effective harmonic mitigation and power quality improvements without requiring battery support. The main objective of SAPF is to mitigate THD from the source connected to a non-linear load. However, enhancing the SAPF's control system can also help reduce other PQIs, such as voltage regulation, PF correction, and improvement in dynamic behavior, including THD reduction simultaneously.

The time domain, frequency domain, and soft computing approaches of the advanced control schemes for grid-connected SAPFs have been investigated, and it was found that ongoing research focuses on hybridised techniques for simultaneous PQI reduction in grid-connected loads [16]–[21]. However, the control loop of SAPF connected to SEIGs in edge-of-grid scenarios faces additional complexities due to load-induced frequency and voltage fluctuations. Especially due to these disturbances, the generated in-phase and quadrature components (α and β) from the measured three-phase signals get affected. Hence it is essential to generate the (α and β) signals precisely for the PWM signal of SAPF. To control the PWM signals of the SAPF effectively, the reference current is to be sinusoidal, regardless of the load current. It is found that the most effective control strategy for producing the (α and β) signals under single-phase harmonic contaminated distorted grid conditions

The associate editor coordinating the review of this manuscript and approving it for publication was José Miguel Sosa (*Corresponding author: Jotirmoy Samanta*).

Jotirmoy Samanta, R. Sangno, R. Pudur, and Y. Gopal are with Department of Electrical Engineering, National Institute of Technology, Arunachal Pradesh, India (e-mails: jotirmoy.phd22@nitap.ac.in, ralli@nitap.ac.in, rajenpudur@nitap.ac.in, and yatindra.pdf.ee25@nitap.ac.in).

J. C. Rosas-Caro is with Facultad de Ingenieria, Universidad Panamericana, Zapopan, Mexico (e-mail: crosas@up.edu.mx).

is the second-order generalized integrator (SOGI) integrated with ROGI [22]. Further, the SOGI-based controller is improved to a dual enhanced second-order generalized integrator (DESOGI) to reject the DC components as well as the DC offset from the system [23], [24].

In the case of a three-phase system, initially Clarke's transformation is performed after measuring the three-phase current or voltage signal. However, this transformation cannot generate orthogonal signals precisely if the system is more distorted or polluted with harmonics. Hence, the SOGI-based control structure must be modified for three-phase systems, even if the system is unbalanced and contains harmonics. In order to perform optimally in an unbalanced system, the SOGI is transformed to a modified double second order generalized integrator (MDSOGI) [25]. Emerging research works are also focused on the DC-offset rejection of the three phase system, hence transforming the SOGI to a mixed second and third order generalized integrator (MSTOGI) [26], [27]. Moreover, to reject fundamental frequency negative sequence components and higher-order harmonics, the generalized integrator is modified to a higher order (i.e., fourth order) [28]. However, the effectiveness of all these generalized integrator is bound to perform under fixed or minimal changes in frequency. In order to track the angular frequency under variable frequency systems, a phase lock loop (PLL) must be incorporated into the generalized integrator-based control framework. The quasi-type-1 (QT-1) PLL is found to perform well, offering a faster dynamic response and less system settling time [29], [30]. Further, to generate the reference current, the dual fundamental current extraction (DFCE) method can be incorporated due to its simpler implementation [22], [31].

A detailed literature review indicating the advantages of the proposed work is tabulated in Table I. From the existing literature, it is explored that the compensating devices STATCOM and SAPF are capable of mitigating several PQIs simultaneously under a non-linear load connected to the system, where PF is not a major concern. The control structure of the SAPF-based compensating device for the grid-connected systems targets some particular PQIs to mitigate, as elaborated in Table 1. If STATCOM is used as a compensating device for SEIG as proposed in [14], [15], then the battery storage increases the cost of the system. Also, the proposed control scheme of [14], [15] is capable of regulating the terminal voltage of SEIG, but the THD of the system, including the settling time, can also be reduced by improving the control structure. The proposed work of [22] has the ability to mitigate PQIs for single-phase grid-connected systems, where frequency variation is not a major problem. Similarly, the work proposed in [31] is capable of mitigating several PQIs in a three-phase grid connected system under unbalanced load conditions. However, when a $2.2kW$ SEIG edge-of-grid system is connected to a combination of both linear and nonlinear loads, then on increasing the non-linear load, it is observed that the voltage and frequency of the system degrade, as shown in Fig. 1. Also, the current THD decreases, whereas the voltage THD increases, as represented in Fig. 2. Hence, due to fluctuation in frequency, the proposed generalized integrator in [22], [25]–[27], [31] will under-perform, and therefore the in-phase and quadrature signal cannot be generated precisely. Due to this problem, SEIG terminal voltage regulation cannot be achieved. It has also been studied from the literature that increasing the order of the generalized integrator leads to a decrease in the order of harmonics along with an effective removal of DC components from the system. The combination of both SOGI and ROGI is suitable to generate a positive sequence component of the load current. Also, it is suitable for reactive power compensation and PF correction, including THD reduction in a single-phase grid system.

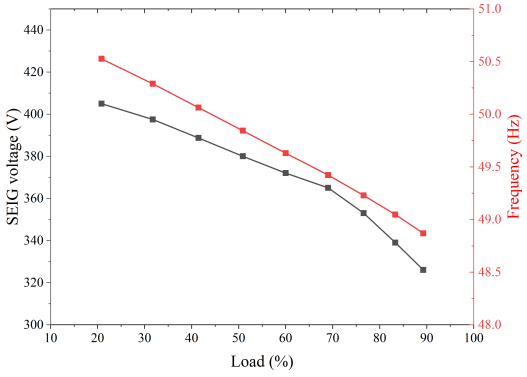

Fig. 1. Voltage and frequency variation with varying load.

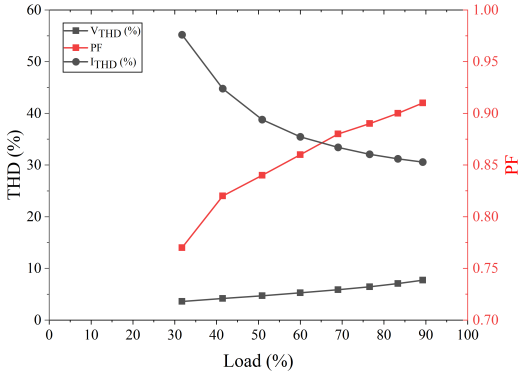

Fig. 2. THD and PF variation with varying load.

Therefore, the proposed research work in this paper utilises SAPF as the compensating device for a $2.2kW$ SEIG as shown in Fig. 3. The control scheme of SAPF utilizes the SOGI base generalized integrator and modifies it to MDSOGI for three-phase edge-off-grid systems in order to mitigate multiple PQIs simultaneously. The tendency of generating perfect sinusoidal in-phase and quadrature signals under dynamic load changes, including system unbalance, is improved by integrating ROGI with MDSOGI. Compared to the other SOGI, MDSOGI, and MSTOGI generalized integrator, hybridizing MDSOGI-ROGI can more effectively dominate the 5^{th} and 7^{th} harmonics. Since there is frequency variation in the edge-of-grid SEIG system, the generalized integrator's efficacy is assessed by integrating with QT-1 PLL. When the SEIG is loaded, the excitation capacitor simultaneously supplies the SEIG with excitation and the SAPF provides reactive power. It had been stated in a prior discussion of this issue that PF correction and voltage regulation cannot be accomplished simultaneously

TABLE I
COMPARISON OF THE PROPOSED METHOD WITH EXISTING LITERATURE

Ref., year	Source	Battery storage	THD (%)	unbalanced load	settling time (s)
[13], 2025	SEIG	×	×	×	0.05
[14], 2024	SEIG	✓	<3.84	✓	1.82
[15], 2024	SEIG	✓	<4.73	✓	1.719
[16], 2021	grid	×	<2.33	✓	×
[18], 2021	grid	×	3.37	×	×
[19], 2022	grid	×	2.756	×	×
[22], 2020	grid	×	<3.5	×	0.04
[23], 2025	grid	×	3.66	×	×
[31], 2022	grid	×	<2.29	✓	0.1
[32], 2025	grid	×	<3.58	✓	×
Proposed work	SEIG	×	<2.35	✓	0.56

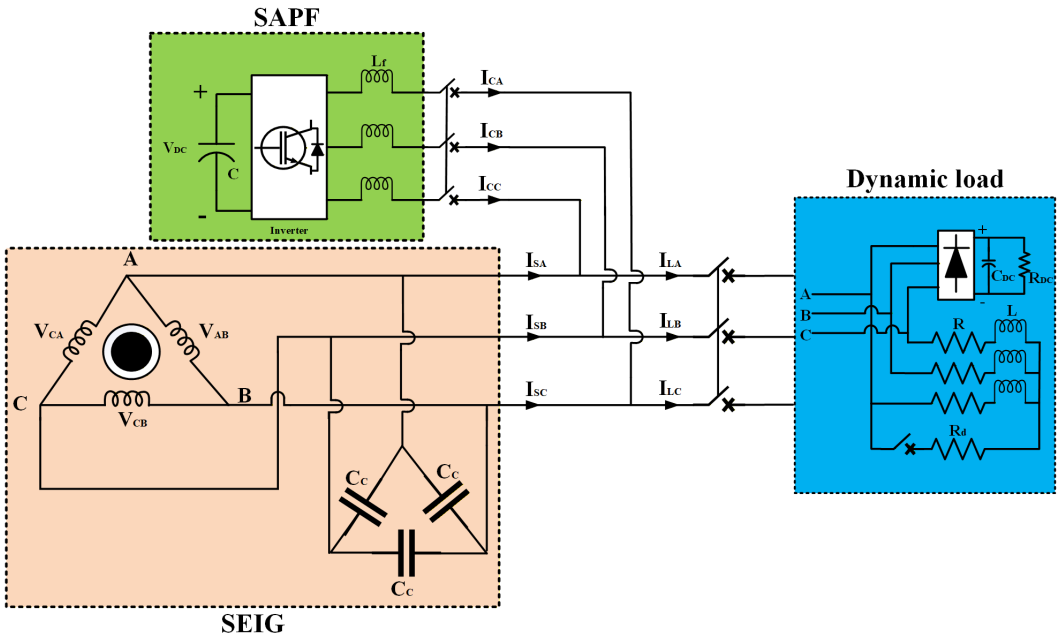

Fig. 3. System schematic diagram.

[33]. Therefore, in this paper under load variation, the SEIG terminal voltage regulation between (420 to 450)V is achieved. The major contribution of the proposed work are:

1) The proposed control scheme efficiently mitigates multiple PQI issues simultaneously, including voltage regulation, harmonics reduction, and power factor correction, ensuring stable and improved performance.
2) Unlike SOGI, MDSOGI and MSTOGI based control schemes, the MDSOGI-ROGI control scheme performance is found to be better under unbalanced loaded conditions. Also, the harmonics elimination of MDSOGI-ROGI under dynamic load changes is analyzed to be better than SOGI, MDSOGI and MSTOGI schemes.
3) The SAPF scheme does not require any battery storage on the DC side, and the DC voltage remains stable even under dynamic load conditions or when the load is removed from the system.
4) Additionally, it demonstrates enhanced adaptability under dynamic load conditions, providing superior operational reliability for SEIG systems. The control approach remains effective even during unbalanced load scenarios, reinforcing its robustness.

This paper is organized into four sections. Section I describes an introduction, including brief literature review. Section II describe the control scheme, including the generation of the reference current for PWM generation. Section III provides a detailed explanation of the results under various dynamic conditions, while Section IV summarizes the conclusions of the proposed work.

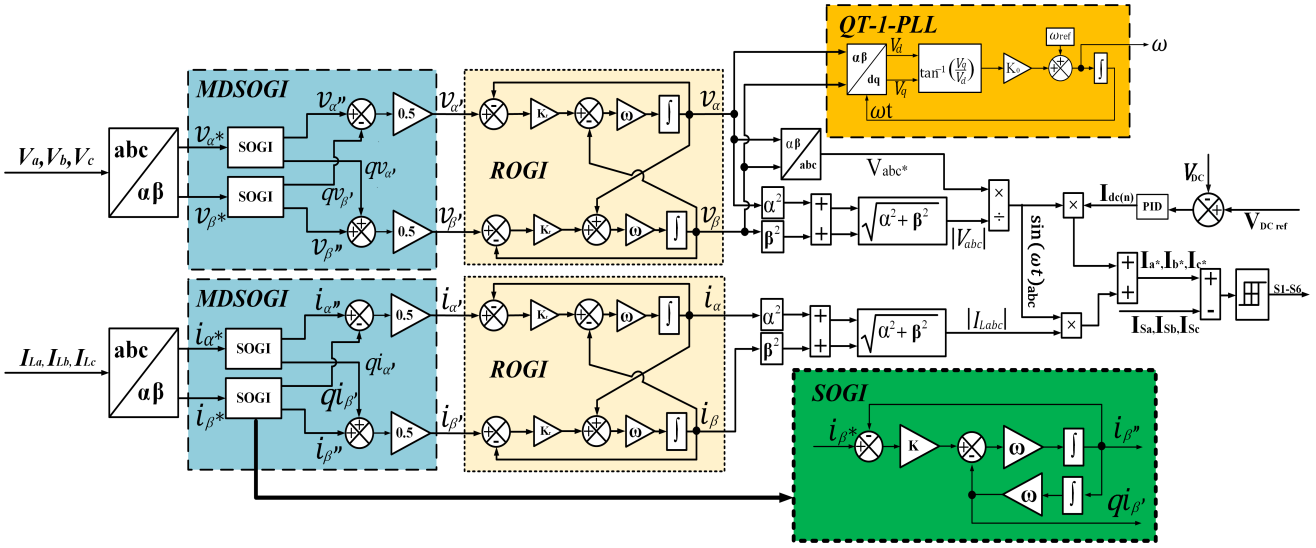

Fig. 4. Proposed control scheme of SAPF with hybridized MDSOGI-ROGI.

II. Control Scheme

The reference current of the control scheme is generated using the DFCE method. To govern the orthogonal signals generated from the three-phase signal, the MDSOGI-ROGI scheme has been proposed. As in the SEIG based edge-of-grid system there is frequency fluctuation, QT-1 PLL based on MDSOGI-ROGI has been implemented to track the angular frequency. The schematic diagram of the overall control structure is represented in Fig. 4.

A. Proposed MDSOGI-ROGI Scheme

The proposed control scheme utilizes a combination of MDSOGI and ROGI to generate the sinusoidal in-phase and quadrature components of the three phase signal after the Clarke's transformation. Initially, the control loop converts the three-phase signal to an (α and β) reference frame signal using Clarke's transformation as denoted by α^* and β^*. MDSOGI is then used to modify the α^* and β^* signals to α' and β' signals. Since signals α^* and β^* are polluted with harmonics, the MDSOGI scheme is employed to mitigate harmonic attenuation as well as to balance the α^* and β^* signals. The transfer function of MDSOGI is represented in equation (1).

$$MDSOGI(s) = \frac{1}{2}\left\{\frac{k\omega s + j(k\omega^2)}{s^2 + k\omega s + \omega^2}\right\} \tag{1}$$

MDSOGI utilizes two SOGIs, each producing one in-phase component ($v_{\alpha''}$, $v_{\beta''}$, $i_{\alpha''}$, $i_{\beta''}$) and one quadrature component ($qv_{\alpha''}$, $qv_{\beta''}$, $qi_{\alpha''}$, $qi_{\beta''}$) whose equations are presented in equations (2, 3).

$$\frac{v_{\alpha''}(s)}{v_{\alpha^*}(s)} = \frac{i_{\alpha''}(s)}{v_{\alpha^*}(s)} = \frac{v_{\beta''}(s)}{v_{\beta^*}(s)} = \frac{i_{\beta''}(s)}{i_{\beta^*}(s)} = \frac{k\omega s}{s^2 + k\omega s + \omega^2} \tag{2}$$

$$\frac{qv_{\alpha'}(s)}{v_{\alpha^*}(s)} = \frac{qi_{\alpha'}(s)}{i_{\alpha^*}(s)} = \frac{qv_{\beta'}(s)}{v_{\beta^*}(s)} = \frac{qi_{\beta'}(s)}{i_{\beta^*}(s)} = \frac{k\omega^2}{s^2 + k\omega s + \omega^2} \tag{3}$$

The step response of the transfer function (2) is shown in Fig. 5. It can be analyze that if the gain value of SOGI decreases, then the system will encounter more settling time and attenuation. A higher gain value will also increase the systems peak but minimize the settling time.

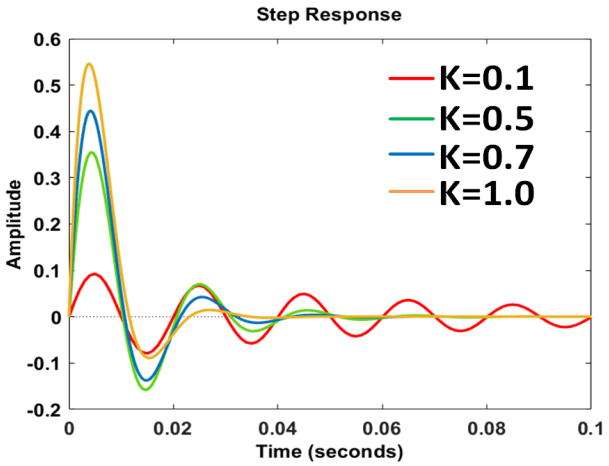

Fig. 5. Step response of SOGI at different gain values.

The ROGI is then used to generate the perfect sinusoidal orthogonal signals α and β signals and equation of ROGI is represented in (4).

$$\frac{v_\alpha(s)}{v_{\alpha'}(s)} = \frac{i_\alpha(s)}{i_{\alpha'}(s)} = \frac{v_\beta(s)}{v_{\beta'}(s)} = \frac{i_\beta(s)}{i_{\beta'}(s)} = \frac{k_r\omega s}{s^2 + 2k_r\omega s + (1+k_r^2)\omega^2} \tag{4}$$

This hybridization enables the system to eliminates the DC components from the three phase signals regardless the harmonics polluted load current. The combined MDSOGI-ROGI transfer function is shown in (5).

$$MDSOGI-ROGI(s) = \frac{0.5\{kk_r\omega^2 s^2 + j(kk_r\omega^3 s)\}}{\omega^2 s^2(2+2kk_r+k_r^2)+\omega^3 s(k+kk_r^2+2k_r)+\omega^4(1+k_r^2)} \quad (5)$$

The selection of the gain values (k and k_r) of MDSOGI-ROGI can be estimated from the bode plot shown in Fig. 6. From Fig. 6a, it is analyzed that increasing k gradually reduces the magnitude curve and reduce the sharpness of the resonance in the MDSOGI-ROGI response, making the filter less selective but more stable. In contrast, raising k_r primarily improves harmonic suppression and deepens the notch at the tuned frequency of $\pm 50Hz$ as shown in Fig. 6b. However, it also introduces a steeper phase shift, indicating stronger attenuation with more dispersive dynamic behavior. In conclusion, k_r determines the depth of attenuation while k controls damping and smoothness. As both values rise, the system approaches a more stable but less sharply selective response with deeper harmonic rejection dependent on k_r strength. Hence for best tracking and harmonics rejection the optimum value of K may be selected between (0.5-0.75) with a variation of K_r between (0.25-0.5).

The step response of MDSOGI-ROGI is compared with SOGI, MDSOGI, MSTOGI scheme, which is represented in Fig. 7. From Fig. 7a, it is observed that SOGI scheme executes highest overshoot with more settling time. Also, due to no imaginary response of SOGI scheme, results in weak quadrature signal. MSTOGI has oscillations but it settles faster than MDSOGI scheme. MDSOGI experiences slow damping with an overshoot, including more settling time. The step response of MDSOGI-ROGI has an overshoot, small oscillation, and stabilizes fastest among all, which indicates the best damping capability. From the comparison of the bode plot as shown in Fig. 8, it is observed that MDSOGI-ROGI scheme provides maximum rejection of unwanted harmonics near $\pm 50Hz$. It is also observed that the MDSOGI-ROGI scheme can accurately extract the fundamental components. Overall it is analyzed that compared to SOGI, MDSOGI, MSTOGI schemes, MDSOGI-ROGI is best suited if there is distortion as well as frequency fluctuation.

The conventional SOGI can achieve strong harmonic attenuation near the fundamental frequency, but it show poor robustness under frequency deviation. This makes it less suitable for unbalanced and dynamic conditions. MSTOGI exhibits enhanced harmonic attenuation across a wider frequency range, while offering less sensitivity to unbalanced loads. Whereas MDSOGI provides a wider bandwidth with improved stability. Also, MDSOGI can minimize the negative sequence components, making it better for unbalanced compensation. The proposed MDSOGI-ROGI improves these properties by integrating adaptive frequency estimation with robust filtering, yielding superior harmonic attenuation and a marked decrease in the unbalance factor, thereby ensuring stable and precise performance in highly distorted and unbalanced systems. The proposed MDSOGI-ROGI improves these properties by integrating adaptive frequency estimation with robust filtering,

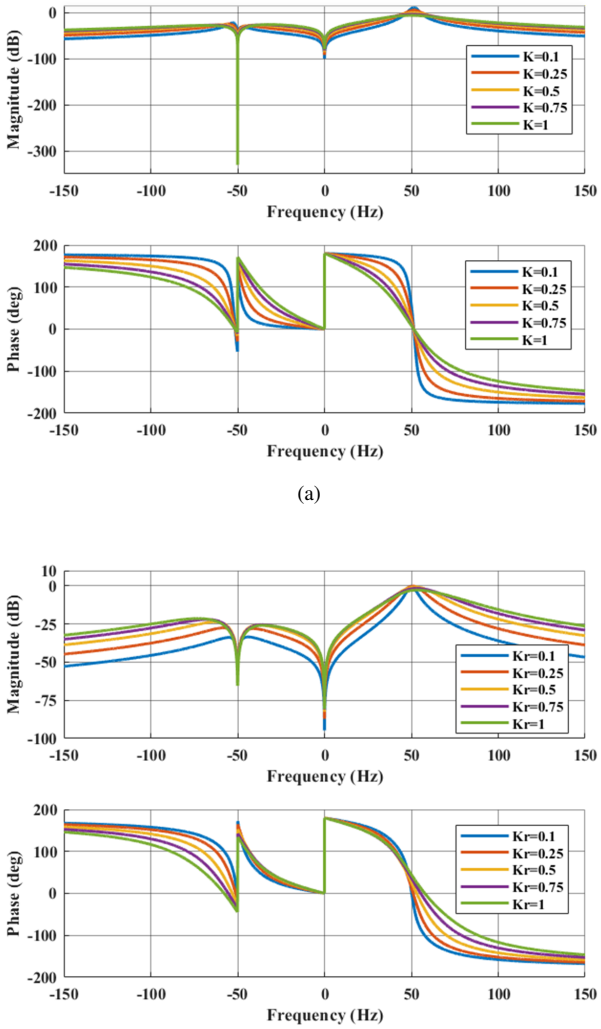

(a)

(b)

Fig. 6. Bode plot of MDSOGI-ROGI. (a) varying k value, (b) varying k_r value

yielding superior harmonic attenuation and a marked decrease in the unbalance factor, thereby ensuring stable and precise effectiveness in highly distorted and unbalanced systems. The computational burden and the mathematical operations that each generalized integrator must perform are indicated by the symbols displayed in Table II. According to the increase of these mathematical operations, the complexity and computational burden of the control scheme also increase. Though the MDSOGI-ROGI scheme exhibits high complexity, but it can mitigate major PQIs in the edge-of-grid system.

B. QT-1 PLL

After applying MDSOGI-ROGI to the three-phase sensed voltage signal, in-phase and orthogonal signals are generated. The system frequency is then estimated using a QT-1 PLL [29]. The phase-error transfer function of the PLL is given by (6).

$$G_e(s) = \frac{\theta_e(s)}{\theta_i(s)} = \frac{1}{1+G_o(s)} \quad (6)$$

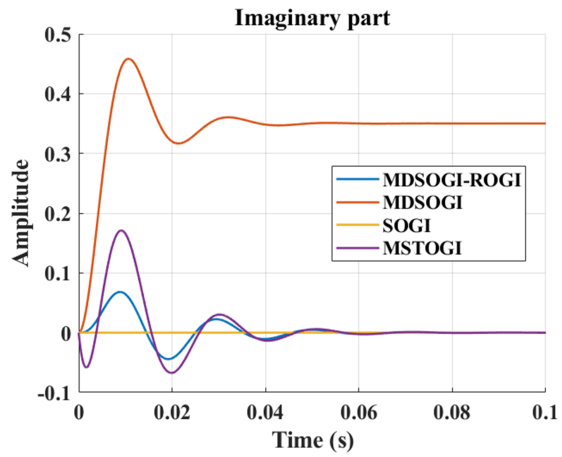

(a)

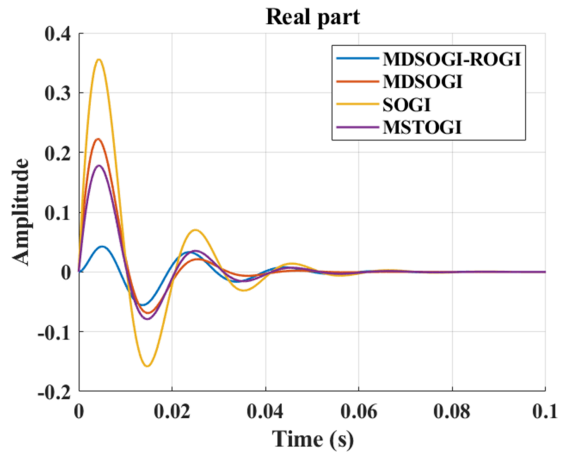

(b)

Fig. 7. Step response comparison of different generalized integrator. (a) Real part, (b) Imaginary part.

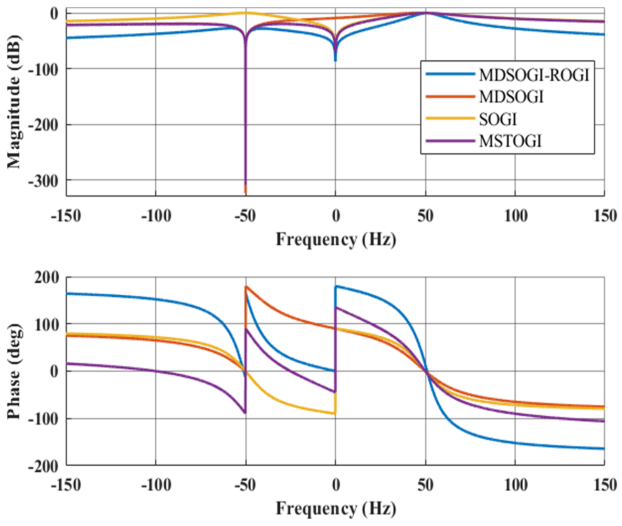

Fig. 8. Comparison of proposed MDSOGI-ROGI phase and magnitude bode plot with MDSOGI, SOGI, MSTOGI scheme.

Where $\theta_e(s)$ is the phase error and $\theta_i(s)$ is the phase input signal. $G_o(S)$ is the open-loop transfer function and can be estimated from (7).

$$G_o(s) = \left(\frac{H(s)}{1-H(s)}\right)\left(1+\frac{k_o}{s}\right) \tag{7}$$

Where k_o is the proportional gain. The selection of k_o is essential for a good stability margin of the PLL [30]. In this paper, the k_o value is selected as 20. DETOGI's transfer function is transformed into a dq-reference frame. The complex transfer function $H(S)$ is then obtained by eliminating the higher-order components in the low-frequency range. Thus $H(S)$ can be obtain from (8).

$$H(s) = \frac{3sk_1 + j2k_1\omega}{s(2(k-1)+j2k_2)+j2\omega k_1} \tag{8}$$

C. Reference Current Generation

To generate the reference current for obtaining the PWM of the SAPF, the DFCE method is employed. The synchronizing component of sin (ωt) can be generated by feeding the sensed three-phase voltage signal to MDSOGI-ROGI from (9).

$$\sin(\omega t)_{abc} = \frac{v_{abc^*}}{\sqrt{v_\alpha^2 + v_\beta^2}} \tag{9}$$

A mathematical operation can estimate the magnitude of the fundamental load current, as shown in (10), which utilizes orthogonal signals (i_α and i_β).

$$|I_{Labc}| = \sqrt{i_\alpha^2 + i_\beta^2} \tag{10}$$

The reference current comprises the fundamental active load currents and the active loss component for mitigating the losses of SAPF, which is formulated in (11).

$$I_{abc^*} = \{I_{dc}(n) + |I_{Labc}|\}\sin(\omega t)_{abc} \tag{11}$$

The losses occurs in SAPF can be evaluated from (12, 13). where k_i and k_i are the proportional and integral gains of PID controller, and $v_{DC}(n)$ is the DC voltage error of SAPF.

$$v_{DC}(n) = V_{DCref} - V_{DC} \tag{12}$$

$$\begin{aligned} I_{dc}(n) = I_{dc}(n-1) + k_p v_{DC}(n) + \\ k_i\left[v_{DC}(n) - v_{DC}(n-1)\right] \end{aligned} \tag{13}$$

III. Result & Discussions

The experiment is performed in real time (OPAL RT-OP4510) and the results are being executed from Keysight's 4-channel DSO. The experimental setup in real time is shown in Fig. 9 and the real time simulation parameters are tabulated in Table III.

TABLE II
COMPUTATIONAL BURDEN

Integrator	$\int$	$\pm$	$\times/\div$	Harmonics attenuation	Unbalance system	Complexity
SOGI [22]	4	4	6	Good	X	Low
MDSOGI [25]	4	6	8	Better	Good	Moderate
MSTOGI [26]	6	8	10	Better	Good	High
MDSOGI-ROGI	6	10	12	Best	Best	High

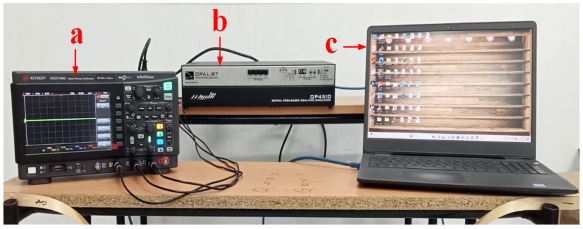

Fig. 9. Experimental setup (a): Keysight Technologies DSOX1204G Digital Oscilloscope Infiniivision 1000 X-Series 4 Channel 70 MHz, 2 $Gsps$, 1 $Mpts$, 5 ns, (b): Opal-RT OP4510 Real-time HIL simulator, (c): Host PC.

TABLE III
SIMULATION PARAMETERS

Real-time simulation parameters	values
Sample time	$10\mu s$
k_p, k_i	0.012, 0.034
$k = k_r$	0.5
K_0	20

A. System Description

This paper presents an edge-of-grid system that uses a $2.2kW$ SEIG as the source. A combination of linear and non-linear dynamic loads is applied to the SEIG to study the overall system's dynamic performance. A three-phase, delta-connected induction machine was connected to a bank of delta-connected capacitors to make it SEIG. Equation (14) represents the minimum capacitance required per phase in the delta configuration [3], [7]. In (14), V_{ph}, f_b, and Q_{SEIG} denote the phase-to-phase voltage, base frequency and reactive power of the induction machine. From equation (14) the capacitance value required is determined as $13\mu F$. The SEIG was set to run at the speed of 1530 RPM, which is at (-2% slip), to run the SEIG at maximum efficiency. During no-load, the terminal voltage and frequency of the SEIG appear to be $430.45V$ and $50.98Hz$.

$$C_{min-delta/phase}(C_c) = \frac{Q_{SEIG}}{3 \times V_{ph}^2 \times 2 \times \pi \times f_b} \tag{14}$$

The PQIs arise due to the dynamic load is reduced by using a SAPF, which consists of a voltage-source inverter connected to a DC link capacitor C on the DC side and a filter inductance L_f in each phase on the AC side. To compensate the real power, the SAPF power must be at least 0.1 per unit of the system's base power. Considering the power of the SEIG as $2.2kW$, the required power of the SAPF should be $220W$. However, the power delivered by SEIG likewise deteriorates, when the speed of SEIG decreases. Hence, to compensate the degraded power, including the mitigation of PQIs simultaneously, the parameters of SAPF can be designed using equations (15, 16, 17) [34]. The DC voltage of the SAPF can be estimated using the modulation index (m) and the system voltage between the two phases (V_s), as shown in equation (15).

$$V_{DC} = \frac{2\sqrt{2}V_S}{\sqrt{3}m} \tag{15}$$

The DC-link capacitor can be calculated from (16).

$$C = \frac{3V_S I_S t}{[(V_{DC})^2 - (V_{DCm})^2]} \tag{16}$$

Where, I_s is the current to be supplied from the SAPF, V_{DCm} is the minimum DC voltage of the SAPF, and t is the SAPF response time and compensating power that the SAPF must provide for a single AC cycle, which can be considered to be $20ms$ [12], [34]. The V_{DCm} can be estimated by assuming an 8% dip in the DC voltage (i.e., for $700V$, it will be $644V$). The L_f value can be calculated from (17), where a is the current rating, which varies between 120% and 180% during transients.

$$L_f = \frac{\sqrt{3}mV_{DC}}{12af_s i_{cpp}} \tag{17}$$

The ripple current i_{cpp} through the filter inductance is allowed to be 5%. The design parameters of the SAPF are elaborated in Table IV.

TABLE IV
SAPF DESIGN PARAMETERS

Design parametrs	values
DC voltage	$700V$
Switching frequency (f_s)	$20kHz$
Rating factor (a)	1.25
Modulation index (m)	0.9
Ripple current (i_{cpp})	$0.25A$

B. Real Time Results

The SEIG-based edge-of-grid system is examined under various dynamic loading conditions. The real-time results of all three phases under load variation are displayed in Fig. 10 and 11. The real time results displayed in Fig. 10 and 11 are converted to per unit of the actual voltage and current signals. All the currents and voltages signal shown in Fig. 10 are of $10A$ and $10V$ amplitude corresponding to the actual

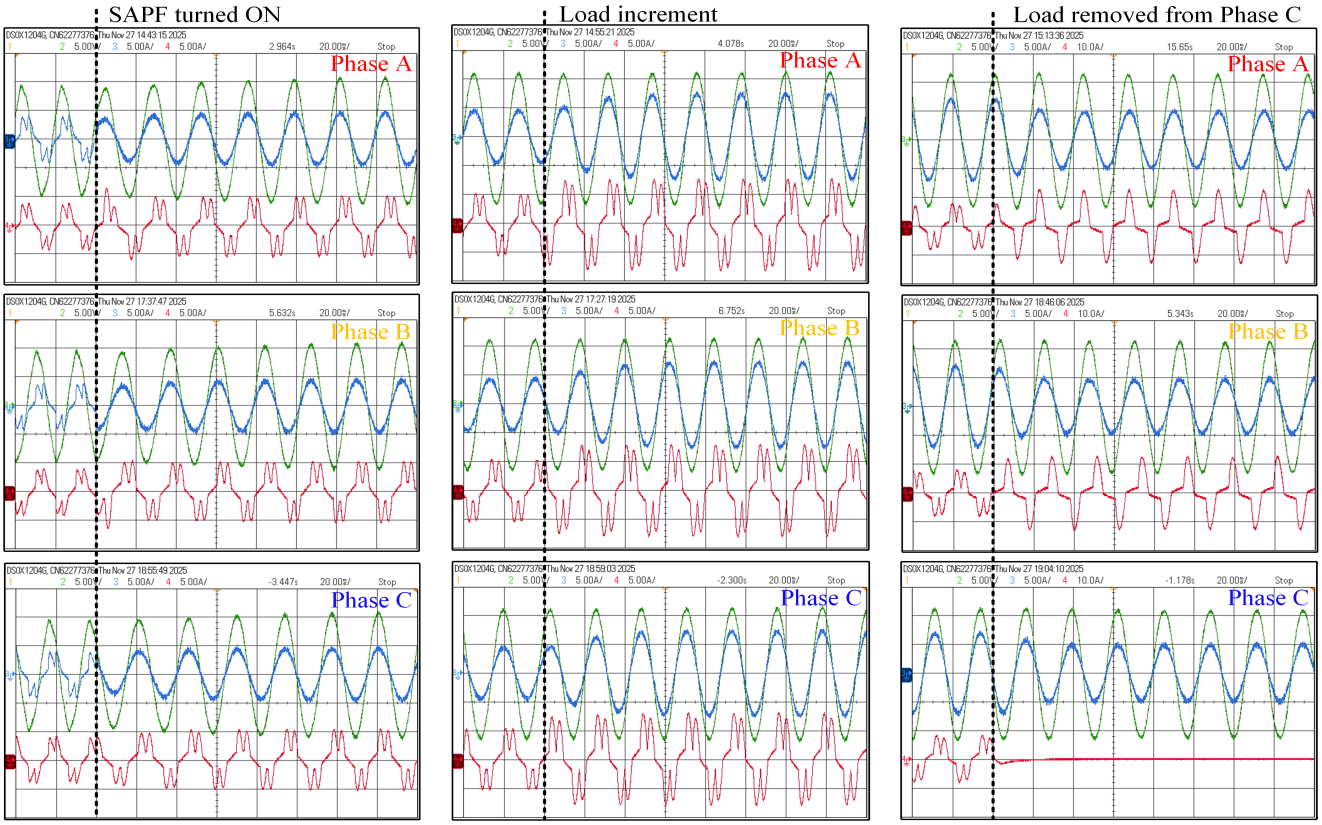

Fig. 10. Real-time result for dynamic and unbalanced loaded condition [$ch-2$ (*green colour*): SEIG terminal voltage, $ch-3$ (*blue colour*): source current, $ch-4$ (*red colour*): load current] (a) during SAPF turned ON, (b) when load is increased, (c) during unbalanced loaded condition.

magnitude level. The result represented in Fig. 10a, indicates both uncompensated results and the result after compensating from the SAPF. The load is increased and made unbalanced once the SAPF is connected to the system, and the results are presented in Fig. 10b, 10c. The corresponding RMS values of the three-phase SEIG voltages, including the DC voltage of SAPF, under dynamic load variations are shown in Fig. 11.

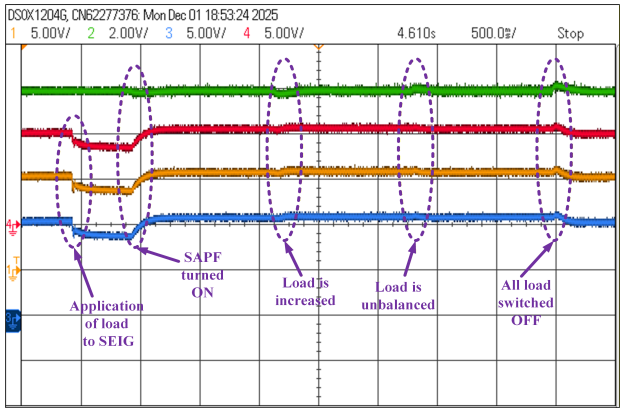

Fig. 11. DC-link voltage of SAPF and RMS voltage of SEIG. $ch-1$ (*yellow colour*): RMS voltage of phase B, $ch-2$ (*green colour*): DC- link voltage, $ch-3$ (*blue colour*): RMS voltage of phase C, $ch-4$ (*red colour*): RMS voltage of phase A.

When the load is connected to the system, it is observed taht the terminal voltage of the SEIG is degraded to $358.6V$, and an increase in load current THD to 34.37%. After introducing SAPF to the system the voltage increases to $445V$ and the source current THD is reduced to 0.91%. During the increment of the load by switching ON (R_d), shown in Fig. 3, the voltage degrades to $321V$, without compensating from SAPF. The terminal voltage and load current THD of SEIG appear to be 5.07% and 28.83%, respectively. From Fig. 10b, it is analyzed that after compensating with the SAPF, the terminal voltage of SEIG and source current THD are reduced to 0.14% and 0.74%, respectively. Also the the terminal voltage of the SEIG increases to $450V$, as analyzed from Fig. 11.

An unbalanced loaded condition is also performed in the system by removing the load from phase C. During an unbalanced loaded condition, the terminal voltage of phase (A, B, C) reduced to $366.1V$, $367.5V$, $394.4V$, without SAPF. The THD of the voltage of phase (A, B, C) increases to 19.03%, 11.37%, 7.34% and the THD value of the load current of phase (A and B) increased to 24.99%. However, through SAPF, the terminal voltage is maintained between (445 to 448)V under an unbalanced loaded condition, as shown in Fig. 11. After connecting SAPF to the system, the THD of voltage of phase (A, B, C) is reduced to 0.30%, 0.27%, 0.46%, and the THD of source current is corrected to 2.15%, 2.35%, 2.02%

for phase (A, B, C), respectively. From The DC-link voltage of the SAPF remains stable at $700V$ when the load is turned off, and the SEIG terminal voltage is maintained at $420V$, as shown in Fig. 11. Additionally, after connecting the SAPF, the PF is also modified from 0.7 to closer to unity. In various dynamic performances, it is noted that the settling time of the overall system is less than $0.56s$.

Furthermore, it can be inferred that after connecting SAPF to the system, the terminal voltage of SEIG can be maintained between (420-450)V, under dynamical load variations. The PF is maintained nearly at unity. The THD of source voltage and current is maintained below 5%. Additionally, it is observed that the source side of the SEIG remains balanced, despite being connected to an unbalanced load. The overall settling time of the system is below $0.56s$, with a maximum overshoot of 2.2% of DC-link voltage, that occurs during load shedding. The results of SEIG at different loading conditions is summarized in Table V.

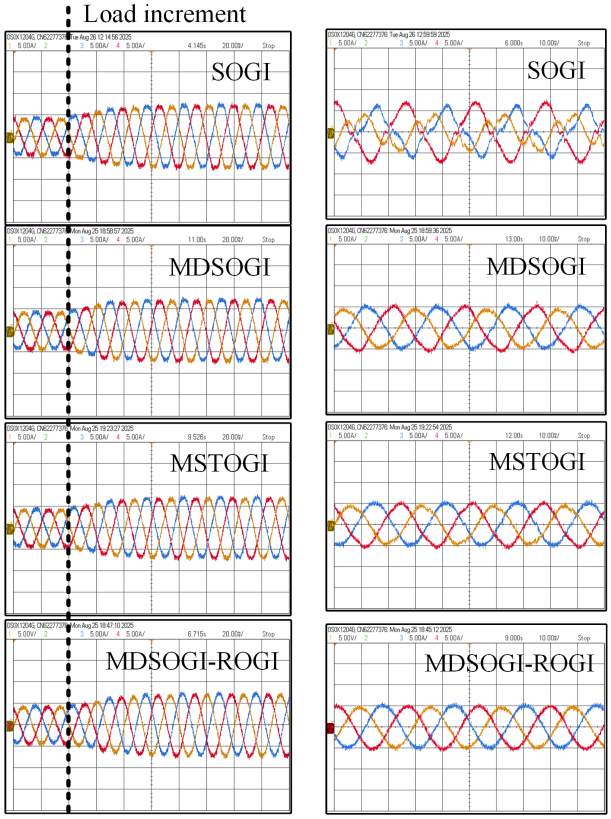

(a) (b)

Fig. 12. Comparison of three-phase source current waveforms using SOGI, MDSOGI, MSTOGI, and MDSOGI-ROGI control scheme: (a) during load increment and (b) under unbalanced load conditions.

C. Comparative Analysis

The MDSOGI-ROGI based control scheme has also been compared with existing SOGI, MDSOGI, MSTOGI techniques to prove its effectiveness. It is found that in the control schemes, PLL is the most vital component to be implemented for the edge-of-grid system where there is a deviation in frequency. Without tracking the angular frequency of the source and implementing it to generate α and β signals, the entire control loop will under perform. The comparison of the different generalized integrator performance under balanced load increment condition is illustrated Fig. 12a. It is observed that MDSOGI-ROGI scheme is capable of eliminating 5^{th} and 7^{th} harmonics better than SOGI, MDSOGI and MSTOGI schemes. The detailed harmonics analysis under balanced

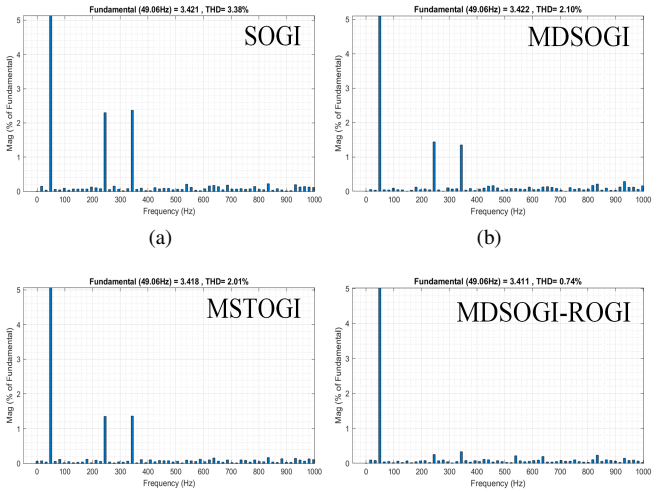

(a) (b) (c) (d)

Fig. 13. Harmonics spectrum of source current after compensation using different generalized integrator control scheme. (a) SOGI, (b) MDSOGI, (c) MSTOGI, (d) MDSOGI-ROGI.

TABLE V
RESULT SUMMARY

Status	Events	PQI	Phase A	Phase B	Phase C
without SAPF	Application of load	PF	0.777	0.777	0.777
		I_s THD (%)	34.37	34.37	34.37
		V_s THD (%)	5.07	5.07	5.08
		V_{RMS} (V)	358.6	358.6	358.6
	Load increment	PF	0.828	0.828	0.828
		I_s THD (%)	28.83	28.77	28.83
		V_s THD (%)	5.07	5.07	5.08
		V_{RMS} (V)	321	321	321
	Unbalanced load	PF	0.829	0.79	–
		I_s THD (%)	24.99	24.99	–
		V_s THD (%)	19.03	11.37	7.34
		V_{RMS} (V)	366	367.8	394.5
with SAPF	SAPF turned ON	PF	0.995	0.995	0.995
		I_s THD (%)	0.91	0.9	0.87
		V_s THD (%)	0.11	0.12	0.14
		V_{RMS} (V)	445	445	445
	Load increment	PF	0.997	0.997	0.997
		I_s THD (%)	0.74	0.77	0.74
		V_s THD (%)	0.13	0.14	0.13
		V_{RMS} (V)	450	450	450
	Unbalanced load	PF	0.99	0.99	0.99
		I_s THD (%)	2.15	2.35	2.02
		V_s THD (%)	0.30	0.27	0.46
		V_{RMS} (V)	446.58	447.1	447.98

TABLE VI
COMPARISON OF HARMONICS ANALYSIS

Harmonics Parameters		Without SAPF	SOGI	MDSOGI	MSTOGI	MDSOGI-ROGI
5^{th}	**THD**$_v$ (%)	4.94	0.55	0.36	0.30	0.04
	THD$_i$ (%)	25.12	2.3	1.44	1.35	0.25
7^{th}	**THD**$_v$ (%)	1.02	0.31	0.18	0.18	0.07
	THD$_i$ (%)	9.25	2.37	1.35	1.36	0.33
11^{th}	**THD**$_v$ (%)	0.56	0.01	0	0.01	0.01
	THD$_i$ (%)	9.06	0.21	0.08	0.09	0.22
Total Harmonics	**THD**$_v$ (%)	5.08	0.65	0.41	0.36	0.13
	THD$_i$ (%)	28.83	3.38	2.10	2.01	0.74

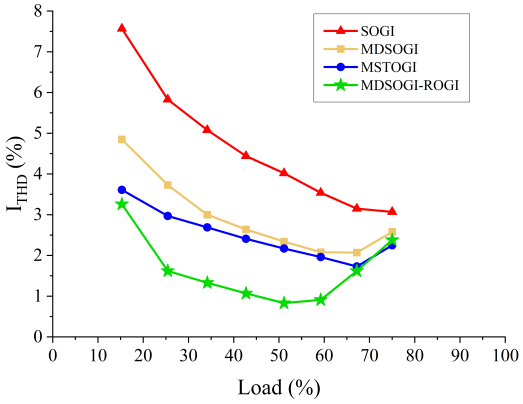

Fig. 14. Source current THD variation results after compensation.

load increment is tabulated in Table VI and the harmonics spectrum is represented in Fig. 13. When the control schemes are introduced for unbalanced loaded conditions, then the SOGI-based scheme cannot make the system balance. In contrast, MDSOGI, MSTOGI and MDSOGI-ROGI can make the system balance as represented in Fig. 12b. Although, the MDSOGI and MSTOGI schemes will produce more harmonics than the MDSOGI-ROGI scheme. Additionally, one phase will produce less power under the MDSOGI and MSTOGI scheme compared to the MDSOGI-ROGI scheme. It is inferred that MDSOGI-ROGI based control schemes have the best capability of eliminating harmonics compared to the SOGI, MDSOGI, MSTOGI scheme under varying loaded conditions, as represented in Fig. 14. Since the QT-1 PLL is incorporated in all the schemes, the MDSOGI–ROGI provides superior harmonic suppression up to approximately 70% of the rated load, resulting in lower THD compared to other generalized integrators within this operating range. From Fig. 14, it is analyzed that under balanced conditions, MDSOGI-ROGI and MSTOGI schemes show almost identical THD performance beyond this loading threshold, while the edge-of-grid SEIG system has a notable frequency drop (below $49Hz$). However, as Fig.12b makes evident, that the MDSOGI–ROGI consistently performs better than the MSTOGI under unbalanced load situations, providing superior system balancing and enhanced harmonic suppression. Furthermore, the research work presented in [14], [15] reported a settling time of $1.8s$ for the SEIG-based edge-of-grid system, whereas in this proposed work, using the MDSOGI-ROGI scheme, the settling time reported was less than $0.56s$.

IV. CONCLUSION

The PQI of SEIG in a standalone system is mitigated using SAPF. The MDSOGI-ROGI control scheme demonstrated its effectiveness in responding to dynamic voltage and frequency variations of the SEIG. The THD of voltage and current of SEIG has been reduced to below 5%, as per the IEEE 519-2022 standard, and PF is improved to 0.99, which is near unity PF. The settling time of the system is minimized below $0.56s$. The voltage of the SEIG has been regulated by (420 to 450)V after compensation from SAPF. Furthermore, under the unbalanced condition, the system becomes balanced after compensation. Future work will focus on the hybrid MDSOGI–ROGI control scheme to be implemented in real time on hardware. The major goals will be to maintain the frequency at $50Hz$ and the SEIG terminal voltage at $415V$, and make it feasible for a standalone renewable energy system.

APPENDIX

A. *Parameters of 2.2 kW, 415 V, 50 Hz, △- connected, 4-pole induction machine developed as SEIG in simulation:*
R_s= 3.81 Ω, R_r= 2.87 Ω, X_ls= X_lr= 4.45 Ω, X_m= 87.010 Ω

B. *Parameters of SAPF:*
DC-link capacitor (C)= 470 μF, Filter inductor (L_f)= 15 mH

C. *Load parameters:*
C_{DC}= 100 μF, R_{DC}= 650 Ω, R_d= 650 Ω, R= 350 Ω, L= 600 mH

REFERENCES

[1] V. Saini and S. K. Singal, "Design and optimization of an off-grid integrated renewable energy system for remote rural electrification in India," *Microsystem Technologies*, vol. 30, pp. 1201–1215, 2024, doi: 10.1007/s00542-024-05625-y

[2] V. B. Murali Krishna, V. Sandeep, S. S. Murthy, and K. Yadlapati, "Experimental investigation on performance comparison of self excited induction generator and permanent magnet synchronous generator for small scale renewable energy applications," *Renewable Energy*, vol. 195, pp. 431–441, 2022, doi: 10.1016/j.renene.2022.06.051

[3] J. Samanta, S. Chakraborty, R. Sangno, and R. Pudur, "Study of power quality issues in a renewable-driven self-excited induction generator due to different loads at edge-off grid system," *e-Prime-Advances in Electrical Engineering, Electronics and Energy*, vol. 11, p. 100885, 2024, doi: 10.1016/j.prime.2024.100885

[4] V. Bala Murali Krishna and S. Vuddanti, "Identification of the best topology of delta configured three phase induction generator for distributed generation through experimental investigations," *International Journal of Emerging Electric Power Systems*, vol. 23, no. 3, pp. 329–341, 2022, doi: 10.1515/ijeeps-2021-0064

[5] V. B. Murali Krishna, S. S. S. R. Sarathbabu Duvvuri, P. V. S. Sobhan, K. Yadlapati, V. Sandeep, and B. K. Narendra, "Experimental study on excitation phenomena of renewable energy source driven induction generator for isolated rural community loads," *Results in Engineering*, vol. 21, p. 101761, 2024, doi: 10.1016/j.rineng.2024.101761

[6] L. Varshney, A. S. Vardhan, A. S. Vardhan, S. Kumar, R. K. Saket, and P. Sanjeevikumar, "Performance characteristics and reliability assessment of self-excited induction generator for wind power generation," *IET Renewable Power Generation*, vol. 15, no. 9, pp. 1927–1942, 2021, doi: 10.1049/rpg2.12116

[7] M. K. Rajak, J. Samanta, and R. Pudur, "A hardware-based novel approach for parallel operation of two differently rated SEIGs," *Results in Engineering*, vol. 17, p. 100825, 2023, doi: 10.1016/j.rineng.2022.100825

[8] U. K. Kalla, B. Singh, S. S. Murthy, C. Jain, and K. Kant, "Adaptive sliding mode control of standalone single-phase microgrid using hydro, wind, and solar PV array-based generation," *IEEE Transactions on Smart Grid*, vol. 9, no. 6, pp. 6806–6814, 2017, doi: 10.1109/TSG.2017.2723845

[9] U. K. Kalla, B. Singh, and S. S. Murthy, "Slide mode control of microgrid using small hydro driven single-phase SEIG integrated with solar PV array," *IET Renewable Power Generation*, vol. 11, no. 11, pp. 1464–1472, 2017. doi: 10.1049/iet-rpg.2016.0089

[10] Y. Bendjeddou, A. Deboucha, L. Bentouhami, E. Merabet, and R. Abdessemed, "Super twisting sliding mode approach applied to voltage orientated control of a stand-alone induction generator," in *Protection and Control of Modern Power Systems*, vol. 6, no. 2, pp. 1–9, 2021. doi: 10.1186/s41601-021-00201-2

[11] C. D. Sanjenbam, B. Singh, and P. Shah, "Power Quality Enhancement of Stand-Alone Hydro Power Generation System Using UPQC," in *IEEE Transactions on Industrial Informatics*, 2024, doi: 10.1109/TII.2024.3413362

[12] B. Singh, S. S. Murthy, and S. Gupta, "Analysis and design of STATCOM-based voltage regulator for self-excited induction generators," in *IEEE Transactions on Energy Conversion*, vol. 19, no. 4, pp. 783–790, 2004, doi: 10.1109/TEC.2004.827710

[13] Guo, H., Gong, P., Xu, Q., Ling, C., Zhang, Z. and Xu, Y., "A NDO-Backstepping Current Tracking Method for SEIG-STATCOM," in *IEEJ Transactions on Electrical and Electronic Engineering*, 2025, doi: 10.1002/tee.70198

[14] B. Dawar, S. R. Arya, and R. Chilipi, "Enhancing power quality with optimized PI controller in three-phase four-wire wind energy system," *Electrical Engineering*, pp. 1–19, 2024. doi: 10.1007/s00202-024-02338-3

[15] B. Dawar, S. R. Arya, and P. Ray, "Wind energy conversion system using fractional least means fourth-based control for power quality," *Electrical Engineering*, pp. 1–17, 2024. doi: 10.1007/s00202-024-02891-x

[16] M. Bajaj, A. Flah, M. Alowaidi, N. K. Sharma, S. Mishra, and S. K. Sharma, "A Lyapunov-function based controller for 3-phase shunt active power filter and performance assessment considering different system scenarios," *IEEE Access*, vol. 9, pp. 66079–66102, 2021, doi: 10.1109/ACCESS.2021.3075274

[17] Guerrero-Rodríguez, N.F., Nunez-Ramirez, V., Batista-Jorge, R.O., Mercado-Ravelo, R., Ramírez-Rivera, F.A., Ferreira, J.A. and Reyes-Archundia, E., "Modelling real non-linear loads for a Controller Hardware-in-the-Loop configuration to evaluate a Shunt Active Power Filter," in *Energy Reports*, vol. 12, pp.1947-1976, 2024, doi: 10.1016/j.egyr.2024.07.056

[18] S. Ouchen, M. Benbouzid, F. Blaabjerg, A. Betka, and H. Steinhart, "Direct power control of shunt active power filter using space vector modulation based on supertwisting sliding mode control," *IEEE Journal of Emerging and Selected Topics in Power Electronics*, vol. 9, no. 3, pp. 3243–3253, 2020, doi: 10.1109/JESTPE.2020.3007900

[19] Z. Li, M. Ren, Z. Chen, G. Liu, and D. Feng, "A bi-sliding mode PI control of DC-link voltage of three-phase three-wire shunt active power filter," *IEEE Journal of Emerging and Selected Topics in Power Electronics*, vol. 10, no. 6, pp. 7581–7588, 2022, doi: 10.1109/JESTPE.2022.3168313

[20] A. A. Valdez-Fernandez, K. O. Mtepele, D. U. Campos-Delgado and G. Escobar, "A generalized model-based controller for the n-level CHB multilevel converter used as a shunt active filter," 2015 *IEEE International Autumn Meeting on Power, Electronics and Computing* (ROPEC), Ixtapa, Mexico, 2015, doi: 10.1109/ROPEC.2015.7395086

[21] Neto, R.C., Neves, F.A. and Souza, H.E.D., "Complex controllers applied to space vectors: A survey on characteristics and advantages," in *Journal of Control, Automation and Electrical Systems*, vol. 31, no. 5, pp.1132-1152, 2020, doi: 10.1007/s40313-020-00623-7

[22] H. Saxena, A. Singh, and J. N. Rai, "Analysis of SOGI-ROGI for synchronization and shunt active filtering under distorted grid condition," in *ISA Transactions*, vol. 109, pp. 380–388, 2021, doi: 10.1016/j.isatra.2020.10.025

[23] Hmad, J., Bendib, A., Echalih, S., Ziane, D., Houari, A. and Rezk, H., "Improved harmonics estimation schemes-based shunt active power filter for quality enhancement under high distortions," in *Electric Power Systems Research*, vol. 246, p.111657, 2025. doi: 10.1016/j.epsr.2025.111657

[24] Semwal, P., Narayanan, V., Singh, B. and Panigrahi, B.K., "Performance Investigation of Hybrid Shipboard Microgrid using ESOGI-FLL Technique," in *e-Prime-Advances in Electrical Engineering, Electronics and Energy*, vol. 7, p. 100437, 2024, doi: 10.1016/j.prime.2024.100437

[25] P. Semwal, V. Narayanan, B. Singh and B. K. Panigrahi, "Performance Evaluation of Power Quality in Shipboard Microgrid Under Different Working Conditions," in *IEEE Transactions on Industry Applications*, vol. 60, no. 2, pp. 2685-2696, 2024, doi: 10.1109/TIA.2023.3348774

[26] C. Zhang, X. Zhao, X. Wang, X. Chai, Z. Zhang and X. Guo, "A Grid Synchronization PLL Method Based on Mixed Second- and Third-Order Generalized Integrator for DC Offset Elimination and Frequency Adaptability," in *IEEE Journal of Emerging and Selected Topics in Power Electronics*, vol. 6, no. 3, pp. 1517-1526, 2018, doi: 10.1109/JESTPE.2018.2810499

[27] M. Kashif and B. Singh, "Interactive Solar Water Pumping Unit With Enhanced Frequency Locked Loop-Based Synchronization for Smart Residential Prosumers," in *IEEE Transactions on Consumer Electronics*, vol. 70, no. 1, pp. 597-607, 2024, doi: 10.1109/TCE.2024.3351691

[28] P. Semwal, V. Narayanan, B. Singh and B. K. Panigrahi, "DHOGI-QT2-PLL-Based Control Scheme for Seamless Mode Transfer in Hybrid Shipboard Microgrid Under Adverse Grid Conditions," in *IEEE Transactions on Consumer Electronics*, vol. 71, no. 1, pp. 1733-1743, 2025, doi: 10.1109/TCE.2024.3503997

[29] P. Semwal, V. Narayanan, B. Singh and B. K. Panigrahi, "Application of an Enhanced Generalized Integrator Based Control for an Emission-Free Marine Microgrid With Shore Grid Synchronization," in *IEEE Transactions on Transportation Electrification*, vol. 11, no. 1, pp. 2988-2999, Feb. 2025, doi: 10.1109/TTE.2024.3432733

[30] N. Muraleedharan and M. K. Mishra, "LVRT Operation With Power Management Strategy for Dual Voltage Source Inverter in Grid-Interfaced Systems," in *IEEE Journal of Emerging and Selected Topics in Power Electronics*, vol. 13, no. 5, pp. 6403-6415, Oct. 2025, doi: 10.1109/JESTPE.2025.3596077

[31] A. K. Dubey, J. P. Mishra, and A. Kumar, "Modified CCF based shunt active power filter operation with dead-band elimination for effective harmonic and unbalance compensation in 3-phase 3-wire system," in *IEEE Transactions on Power Delivery*, vol. 37, no. 3, pp. 2131-2142, 2021. doi: 10.1109/TPWRD.2021.3104828

[32] Liu, J., Wan, L., Hu, K., Xu, Z. and Wang, F., "A reference current control strategy based on Sogi and FBD method for shunt active power filter," in *Electrical Engineering*, vol. 107, no. 1, pp.133-142, 2025, doi: 10.1007/s00202-024-02521-6

[33] Chandra A, Singh B, Singh BN, Al-Haddad K., "An improved control algorithm of shunt active filter for voltage regulation, harmonic elimination, power-factor correction, and balancing of nonlinear loads," in *IEEE transactions on Power electronics*, vol. 15, no. 3, pp. 495-506, May 2000, doi: 10.1109/63.844510

[34] Kumaresan S, Habeebullah Sait H., "Design and control of shunt active power filter for power quality improvement of utility powered brushless DC motor drives," in *Automatika*, vol. 61, no. 3, pp. 507-521, July 2020, doi: 10.1080/00051144.2020.1789402

Jotirmoy Samanta received his B.Tech. degree in Electrical and Electronics Engineering from S.R.M. Institute of Science and Technology, Chennai, India, in 2020. He has received his M.Tech. degree from National Institute of Technology Arunachal Pradesh, India, in 2022. He is currently pursuing the PhD degree in Electrical Engineering at the National Institute of Technology, Arunachal Pradesh, India. His research interests include power quality improvement, active power filters, renewable energy systems, and control strategies for induction generators.

Ralli Sangno received his B.E in Electrical Engineering from Government Engineering College (GECM), Modasa, Gujarat, India in the year 2006. He has obtained his M. Tech (PSE) from NERIST, Arunachal Pradesh, India in 2009 and awarded PhD from the same Institute in the year 2019. He joined as Assistant Professor in Electrical Engineering Department in NIT AP in the year 2013. He has published extensively in reputed international journals and conferences (Springer, Elsevier, IEEE, Taylor & Francis). Guided multiple Ph.D., M.Tech., and B.Tech. projects, and actively contributed to funded research projects, workshops, and professional development programs. Skilled in academic leadership, community engagement, and campus administration with demonstrated expertise in energy systems, power quality, and MEMS/NEMS converters for renewable energy applications.

Rajen Pudur (Senior Member, IEEE) received his bachelor's degree in electrical engineering from North Gujarat University in 2002, the master's degree in electrical engineering from NERIST in 2011 and received the Ph.D. in Electrical Engineering from NERIST in 2016, respectively. He is currently working as an Associate Professor at the Department of Electrical Engineering, National Institute of Technology Arunachal Pradesh. His research areas include power system, renewable source of energy, power quality issues of renewable energy, micro-hydro power plants, renewable energy integration, IG for rural areas. He has published many papers in reputed journals. He has been serving as a reviewer for many highly-respected journals.

Yatindra Gopal received his B.Tech. Degree in Electrical Engineering from Rajasthan Technical University (RTU), Kota, India in 2010, M.Tech. Degree in Power Electronics and Drives from Kalinga Institute of Industrial Technology (KIIT), Bhubaneswar, India in 2013 and Ph.D. Degree in Power Electronics and Drives from RTU, Kota, India in 2020. He is currently a Post Doctoral Fellow with the Department of Electrical and Electronics Engineering, National Institute of Technology Arunachal Pradesh, India. His Areas of Interest are Power Electronics, Efficient Multilevel Inverters Design, High-Gain Converters, Photovoltaic Systems, Power Quality, and Harmonics Elimination of Multilevel Inverters. He is a regular reviewer of several IEEE, IET, and Wiley journals.

Julio C. Rosas-Caro (Senior Member, IEEE) received his B.S. degree in Electronics Engineering and the M.S. degree in Electrical Engineering from the Tecnologico de Cd. Madero, Mexico. He received the Ph.D. degree in Electrical Engineering from the Centro de Investigación y de Estudios Avanzados del Instituto Politécnico Nacional (Cinvestav del IPN), Mexico. He has been a visiting scholar at several institutions, including Michigan State University, the University of Colorado, Ontario Tech University, the University of Sheffield, and Pennsylvania State University. He has published more than 100 papers in indexed journals and has over 3,700 citations according to Google Scholar. He serves on the editorial team of three indexed journals. His research interests include power electronics, with emphasis on DC–DC converters. Dr. Rosas-Caro is a Professor at Universidad Panamericana, a Senior Member of IEEE, a member of the IET, Sigma Xi, and the Mexican National System of Researchers (Level III).